Energy & Environmental Science

ROYAL SOCIETY OF CHEMISTRY

PAPER

View Article Online
View Journal | View Issue

Cite this: *Energy Environ. Sci.*, 2025, **18**, 702

Triphenylamine–ethylenedioxythiophene copolymers for perovskite solar cells: impact of substituent type and alternation†

Lifei He,‡[a] Yuyan Zhang,‡[a] Bing Zhang,[a] Yanfei Mu,[b] Niansheng Xu,*[a] Yaohang Cai,*[a] Yi Yuan,[a] Jing Zhang,[a] Min Zhang[b] and Peng Wang*[a]

Received 25th July 2024,
Accepted 14th November 2024

DOI: 10.1039/d4ee03316g

rsc.li/ees

Developing cost-efficient p-type polymeric semiconductors with superior quality factors, such as energy levels, hole transport, and mechanical properties, is crucial for the application of n–i–p perovskite solar cells. In this study, we synthesized three triphenylamine–ethylenedioxythiophene alternating copolymers *via* direct arylation polycondensation. The first polymer features three methyl groups on the non-main chain phenyl rings, the second has one 2-octyldodecyloxy group, and the third incorporates a combination of half three methyl groups and half one 2-octyldodecyloxy group. Variations and combinations of these substituents resulted in differences in molecular weights, glass transition temperatures, highest occupied molecular orbital energy levels, and film morphologies. Compared to reference polymers with only one type of substituent, the synergistic use of different substituents led to polymeric semiconductor composite films with smoother morphology and higher conductivity. Utilizing this uniquely substituted p-type polymeric semiconductor, we fabricated perovskite solar cells with an average power conversion efficiency of 25.4%. These cells exhibited excellent stability under thermal storage at 85 °C and operational conditions at 45 °C.

Broader context

Lead iodide-based organic–inorganic hybrid perovskites are exceptional light-absorbing materials for solar cells, achieving impressive power conversion efficiencies. However, n–i–p type perovskite solar cells, which use low-cost tin dioxide as the electron transport layer, currently face significant challenges regarding thermal storage stability and operational durability. Hybrid perovskites tend to decompose when exposed to heat or moisture, and strong local electric fields can induce ion migration. The grain size of high-quality perovskite films can reach the micron level, with root mean square roughness extending to tens of nanometers. To advance the practical application of these solar cells, there is an urgent need to develop p-type organic semiconductor materials that offer excellent film-forming properties, superior hole transport capabilities, high cohesive energy density, and low cost.

1 Introduction

Lead halide-based perovskites have emerged as exceptional light-absorbing materials for solar cells due to their tunable optical bandgaps, extended excited-state lifetimes, and the availability of inexpensive raw materials.[1,2] In fabricating high-efficiency n–i–p perovskite solar cells (PSCs, device structure shown in Fig. S1, ESI†), smooth tin dioxide (SnO_2) thin films are predominantly used as electron transport layers. For hole transport layers (HTLs), the organic semiconductor **spiro-OMeTAD** (chemical structure shown in Fig. S2, ESI†) is frequently employed.[3–5] The **spiro-OMeTAD** molecule comprises four dimethoxytriphenylamine subunits. Extensive p–π conjugation effects lead to a relatively shallow highest occupied molecular orbital (HOMO) energy level (E_H^{DFT}) for **spiro-OMeTAD**, calculated to be −4.49 eV (Fig. S3A, ESI†) by the density functional theory method. Effective doping, achieved *via* air oxidation assisted by fluoroalkylsulfonyl imide salts, results in a hole density of approximately 10^{18} cm^{-3} and a conductivity of several tens of μS cm^{-1}.[6] However, the primary challenge in using HTLs composed of **spiro-OMeTAD** and fluoroalkylsulfonyl imide salts is their poor thermal stability, with a glass transition temperature below 85 °C.[6–9]

[a] *State Key Laboratory of Silicon and Advanced Semiconductor Materials, Department of Chemistry, Zhejiang University, Hangzhou 310058, China. E-mail: nshxu@zju.edu.cn, caiyh@zju.edu.cn, pw2015@zju.edu.cn*

[b] *Institute for New Energy Materials and Low Carbon Technologies, Tianjin University of Technology, Tianjin, 300384, China*

† Electronic supplementary information (ESI) available. See DOI: https://doi.org/10.1039/d4ee03316g

‡ These authors contributed equally to this work.

Compared to molecular semiconductors,[10–12] polymeric semiconductors exhibit longer persistence lengths, with π-electrons delocalized, tunneling, and hopping within the molecule, facilitating intrachain charge transport. Interchain entanglement can form an interpenetrating network, promoting interchain charge transfer.[13–21] The woven structure of polymers imparts superior thermomechanical properties and impermeability to films. Additionally, the rheological characteristics of polymer solutions make them well-suited for high-throughput, large-area solution processing techniques such as inkjet printing and screen printing. Currently, the charge transport performance of some polymeric semiconductors is comparable to that of single-crystal molecular semiconductors. High-mobility polymeric semiconductors typically exhibit a semicrystalline film morphology, which can lead to poor smoothness and potential microscale shunt issues when applied in multilayer diode devices. Donor–acceptor-type polymeric semiconductors usually have narrow optical bandgaps, which may cause dissipative light absorption when used in PSCs. Therefore, it is necessary to design new conjugated backbones to fine-tune the electronic properties (energy levels, hole density, mobility), film morphology, and thermal stability of p-type polymeric semiconductors, aiming to achieve highly efficient and stable cells. To date, a wide range of polymeric semiconductors have been evaluated for PSCs; however, materials that simultaneously offer high efficiency, high stability, and low cost remain scarce.[22–39]

The homopolymer of 2,4,6-trimethyl-*N*,*N*-diphenylaniline (TPA3Me), referred to as **PTAA** (chemical structure shown in Fig. 1A), is also frequently utilized in the fabrication of PSCs.[4,40,41] However, its E_H^{DFT} value of −4.74 eV (Fig. S3A, ESI†) is relatively deep, leading to inadequate hole density and conductivity when attempting to achieve doping *via* air oxidation. Ethylenedioxythiophene (EDOT), a commercially available and cost-effective fine chemical, readily undergoes highly selective palladium-catalyzed activation of the C–H bonds in its thiophene ring.[42–49] Note that C–H activation could occur at the β-position of other thiophene derivations.[50] Periodic boundary condition density functional theory calculations reveal that the alternating copolymer of TPA3Me and EDOT (**p-TPA3Me-E**, Fig. 1A) exhibits an E_H^{DFT} of −4.40 eV, which is 340 meV shallower than that of **PTAA**. Moreover, molecular dynamics simulations indicate that the theoretical glass transition temperature (T_g^{SV}) of **p-TPA3Me-E** is 228 °C, surpassing those of **spiro-OMeTAD** (153 °C) and **PTAA** (118 °C). However, experimental studies indicate that achieving a high molecular weight for **p-TPA3Me-E** is hindered by solubility limitations. To address this challenge, we substituted every other TPA3Me unit in **p-TPA3Me-E** with 4-((2-octyldodecyl)oxy)-*N*,*N*-diphenylaniline (TPAOOD), resulting in the ternary alternating copolymer **p-TPA3Me-E-TPAOOD-E** (Fig. 1A), which possesses an E_H^{DFT} of −4.37 eV (Fig. S3A, ESI†) and a T_g^{SV} of 186 °C (Fig. S3B, ESI†). To systematically elucidate the structure–property–function relationship, we further examined the E_H^{DFT} (−4.34 eV, Fig. S3A, ESI†) and T_g^{SV} (134 °C, Fig. S3B, ESI†) of the copolymer **p-TPAOOD-E** (chemical structure shown in Fig. 1A). Frontier molecular orbital analyses reveal that the HOMOs of **PTAA** and the three triphenylamine–ethylenedioxythiophene alternating copolymers are predominantly localized on the main chain, with comparatively less distribution on the non-main chain phenyl rings (Fig. 1B).

In this study, we synthesized three alternating copolymers of triphenylamine and ethylenedioxythiophene *via* a palladium-catalyzed direct arylation condensation reaction. Experimental results demonstrate that both the type and the alternating use of substituent significantly influence the molecular weight of the polymers produced under identical synthetic conditions.

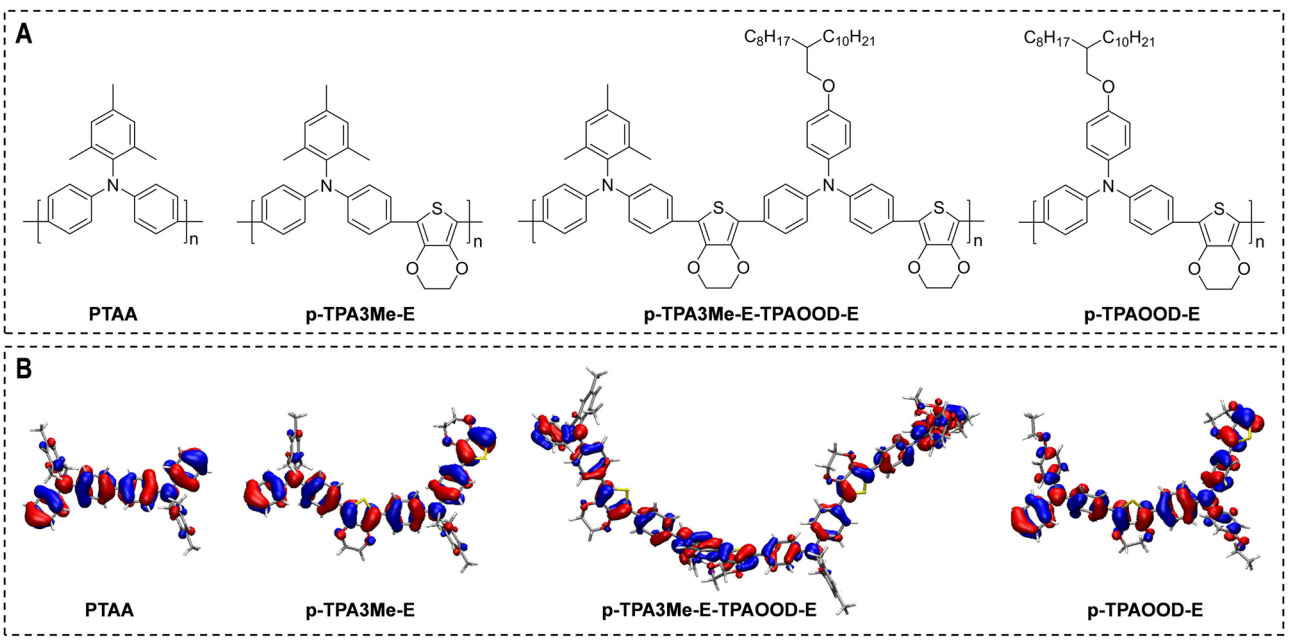

Fig. 1 (A) Chemical structures of four triphenylamine-based polymeric semiconductors. (B) Contour plots of highest occupied molecular orbitals. For computational efficiency, the 2-octyldodecyloxy group was substituted with an ethoxy group. Isovalue: 0.02.

Our findings reveal that the HOMO energy level of polymeric semiconductor is not only correlated with the rate constant for hole extraction from photoexcited formamidinium lead triiodide ($FAPbI_3$) perovskite but also with the hole density generated through air oxidation doping. Notably, both the HOMO energy level and the film morphology of polymeric semiconductor significantly impact the efficiency of PSCs. Utilizing the alternating polymer **p-TPA3Me-E-TPAOOD-E**, we achieved an average efficiency of 25.4%, surpassing those of cells fabricated under the same conditions using **spiro-OMeTAD** (24.1%), **PTAA** (20.5%), **p-TPA3Me-E** (23.2%), and **p-TPAOOD-E** (23.3%). Importantly, the cells based on **p-TPA3Me-E-TPAOOD-E** exhibited excellent stability under thermal storage at 85 °C and operational conditions at 45 °C.

2 Results and discussion

2.1 Synthesis and glass transition

For comprehensive details regarding the synthesis, purification, and structural characterization of the monomers and three alternating copolymers, please refer to Section 1.3 of the ESI.† The monomer *N*,*N*-bis(4-bromophenyl)-2,4,6-trimethylaniline (2Br-TPA3Me) was synthesized following established procedures.[51] Concurrently, diphenylamine underwent Buchwald–Hartwig cross-coupling with 1-bromo-4-(2-octyldodecyloxy)benzene[52] to yield 4-((2-octyldodecyl)oxy)-*N*,*N*-diphenylaniline (TPAOOD). Two-fold bromination of TPAOOD with *N*-bromosuccinimide produced the monomer 2Br-TPAOOD. Subsequently, 2Br-TPAOOD was subjected to two-fold Suzuki–Miyaura cross-couplings with 2-(2,3-dihydrothieno[3,4-*b*][1,4]dioxin-5-yl)-4,4,5,5-tetramethyl-1,3,2-dioxaborolane, resulting in the monomer 4-(2,3-dihydrothieno[3,4-*b*][1,4]dioxin-5-yl)-*N*-(4-(2,3-dihydrothieno[3,4-*b*][1,4]dioxin-5-yl)phenyl)-*N*-(4-((2-octyldodecyl)oxy)phenyl)aniline (E-TPAOOD-E). In the presence of a palladium acetate/tris(cyclohexyl)phosphine catalyst, 2Br-TPA3Me and E-TPAOOD-E were condensed in *N*,*N*-dimethylacetamide to form the alternating copolymer **p-TPA3Me-E-TPAOOD-E**. Under analogous conditions, 2Br-TPA3Me (or 2Br-TPAOOD) reacted with EDOT to yield the copolymer **p-TPA3Me-E** (or **p-TPAOOD-E**). High-temperature gel permeation chromatography analyses revealed number-average molecular weights of 6.23 kDa, 180 kDa, and 242 kDa for **p-TPA3Me-E**, **p-TPA3Me-E-TPAOOD-E**, and **p-TPAOOD-E**, respectively, with polystyrene as the standard. The corresponding polydispersity indices were 1.50, 1.79, and 1.50. The lower molecular weight observed for **p-TPA3Me-E** is attributed to pronounced π–π interactions, which lead to reduced solubility of the polymer. In contrast, the incorporation of flexible substituents significantly enhances the molecular weight of the polymer.

Differential scanning calorimetry (DSC) measurements (Fig. S4, ESI†) revealed glass transition temperatures (T_g^{DSC}) of 185 °C for **p-TPA3Me-E**, 153 °C for **p-TPA3Me-E-TPAOOD-E**, and 108 °C for **p-TPAOOD-E**. Additionally, molecular dynamics simulations were employed to model the specific volume of polymers with an approximate chain molecular weight of 10 kDa across various temperatures during the material design phase. It is well known that molecular weight influences the glass transition temperature of a polymeric semiconductor: at lower molecular weights, glass transition temperature increases with molecular weight, but it levels off around a stable value as the molecular weight approaches 10 kDa. Through linear fitting of the specific volume data in both low- and high-temperature regions, we identified the intersection of the fitted lines corresponding to T_g^{SV}. Notably, our results demonstrate a strong linear correlation between T_g^{DSC} and T_g^{SV} (Fig. S5, ESI†). This study indicates that the incorporation of three methyl groups significantly enhances the polymer's glass transition temperature compared to the bulky flexible substituent 2-octyldodecyloxy. However, the solubility limitations pose challenges in synthesizing high molecular weight materials. The alternating use of these two substituents offers a strategic compromise, effectively modulating the glass transition temperature while regulating the polymer's molecular weight.

2.2 HOMO energy levels: correlation with hole densities and hole extraction kinetics

We first deposited the polymeric semiconductors onto glassy carbon disk electrodes and recorded their thin-film cyclic voltammograms in acetonitrile solution (Fig. S6A–D, ESI†). From the onset potentials of the oxidation waves, we calculated the HOMO energy levels (E_H^{EC}). The results indicated that the E_H^{EC} values for **PTAA**, **p-TPA3Me-E**, **p-TPA3Me-E-TPAOOD-E**, and **p-TPAOOD-E** were −5.37 eV, −5.18 eV, −5.16 eV, and −5.14 eV, respectively. Subsequently, we sequentially deposited a PEDOT:PSS conductive layer and an organic semiconductor layer onto smooth ITO substrates. Atomic force microscopy imaging (Fig. S7, ESI†) revealed that **spiro-OMeTAD**, **p-TPA3Me-E**, **p-TPA3Me-E-TPAOOD-E**, and **p-TPAOOD-E** formed continuous amorphous films with root-mean-square roughness values of 0.37 nm, 0.50 nm, 0.45 nm, and 0.53 nm, respectively. In contrast, the **PTAA** film exhibited poorer integrity with numerous pinholes and a root-mean-square roughness of 0.69 nm. We also observed similar phenomena on the monocrystalline silicon substrate (Fig. S8, ESI†). Notably, in the absence of a PEDOT:PSS interlayer, these organic semiconductors exhibited poorer film-forming properties on both ITO and silicon substrates, likely due to weak interactions. We then conducted ultraviolet photoelectron spectroscopy measurements on the samples. The results showed that the HOMO energy levels (E_H^{UPS}) of **p-TPA3Me-E**, **p-TPA3Me-E-TPAOOD-E**, and **p-TPAOOD-E** films were −5.04 eV, −5.02 eV, and −4.99 eV, respectively (Fig. S9A–C, ESI†). Although the absolute values of the HOMO energy levels obtained from density functional theory calculations, cyclic voltammetry measurements, and ultraviolet photoelectron spectroscopy measurements differed, the relative trends of E_H^{EC}, E_H^{UPS}, and E_H^{DFT} were consistent (Fig. S6E and S9D, ESI†). Next, we spin-coated the polymeric semiconductors onto quartz substrates and measured their UV-vis absorption spectra. By plotting Tauc plots (Fig. S10, ESI†), we determined the optical bandgaps (E_g^{opt}) of **p-TPA3Me-E**, **p-TPA3Me-E-TPAOOD-E**, and **p-TPAOOD-E** films to be 2.65 eV, 2.63 eV, and 2.60 eV, respectively. Combining the E_H^{UPS} and E_g^{opt} values, we calculated the LUMO energy levels of the polymeric

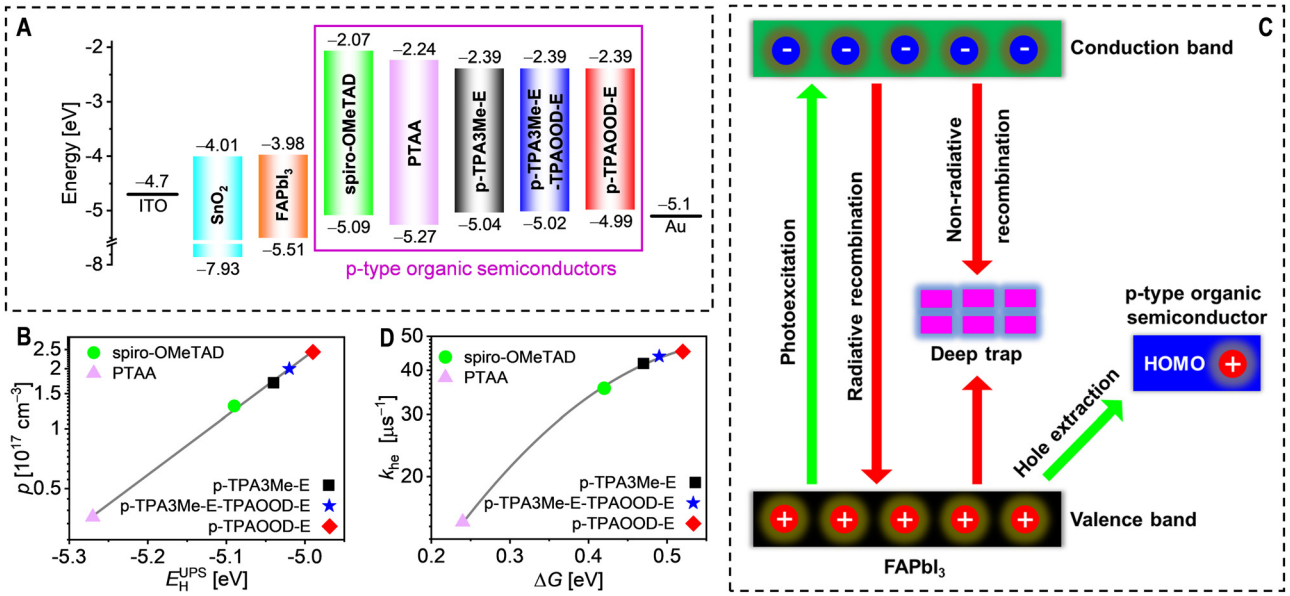

Fig. 2 (A) Energy diagram of various materials in perovskite solar cells. The numbers below and above the colored bars represent the energy levels of the valence band edge (HOMO) and conduction band edge (LUMO), respectively. Work functions of ITO and Au are also indicated. (B) Semi-logarithmic plot of hole density (p) *versus* HOMO energy level (E_H^{UPS}) obtained from ultraviolet photoelectron spectroscopy. The grey solid line indicates a linear fit. (C) Schematic depiction of photoinduced electronic processes in an $FAPbI_3$ film covered with a p-type organic semiconductor. (D) Semi-logarithmic plot of hole extraction rate constant (k_{he}) as a function of driving force (ΔG), defined as the energy difference between the valence band edge of $FAPbI_3$ and the HOMO of the organic semiconductor. The grey solid line represents a nonlinear fit based on Marcus electron transfer theory.

semiconductors. By referencing the work functions of ITO and gold electrodes and the band edges of SnO_2 and $FAPbI_3$ from the literature,[53] we constructed the energy diagram for the n–i–p type PSCs, as shown in Fig. 2A.

Subsequently, we fabricated metal–insulator–semiconductor (MIS) devices using pristine organic semiconductors and measured their impedance spectra under various biases to determine the capacitance of the organic semiconductor layer. Based on the Mott–Schottky relationship, we estimated the hole density (p) in the pristine organic semiconductors, which followed the order: **PTAA** (3.6×10^{16} cm^{-3}) < **spiro-OMeTAD** (1.3×10^{17} cm^{-3}) < **p-TPA3Me-E** (1.7×10^{17} cm^{-3}) < **p-TPA3Me-E-TPAOOD-E** (2.0×10^{17} cm^{-3}) < **p-TPAOOD-E** (2.4×10^{17} cm^{-3}).[49] Details on the fabrication, measurement, and data analysis of MIS devices are provided in Section 1.6 of the ESI.† For intrinsic organic semiconductors, charge carriers are generated *via* thermally activated disproportionation reactions; for materials with optical bandgaps larger than 1.5 eV, the carrier density is below 10^4 cm^{-3}.[54] Therefore, the holes in these pristine organic semiconductors must be generated through other mechanisms. The most likely mechanism is oxidative doping by oxygen in the air, where oxygen acts as a dopant, oxidizing these high-HOMO-energy level organic semiconductors. This process converts a small number of neutral organic semiconductor molecules into their radical cation forms, balanced by peroxide anions generated from the reduction of oxygen. As shown in Fig. 2B, there is a strong linear correlation between the logarithm of the p values and the HOMO energy levels of the organic semiconductors. From a chemical reaction standpoint, the higher the HOMO energy level of the organic semiconductor, the greater the Gibbs free energy change (ΔG_{pd}) for oxidative doping by air, leading to a higher equilibrium constant (K_{pd}) and, consequently, a higher concentration of radical cations (larger p). The relationship between ΔG_{pd} and K_{pd} can be quantitatively described by the equation $\Delta G_{pd} = -RT\ln(K_{pd})$, where R is the gas constant and T is the temperature in Kelvin.

As shown in Fig. 2C, the photogenerated excitons in the $FAPbI_3$ perovskite films undergo both radiative and non-radiative recombination. Holes diffusing to the surface of the perovskite film are extracted by p-type organic semiconductors with sufficiently high HOMO energy levels. The rate constant of the hole extraction process (k_{he}) is primarily dependent on the energy difference (ΔG) between the valence band of the perovskite and the HOMO of the p-type organic semiconductor. The yield of the hole extraction process is determined by k_{he}, the radiative recombination rate constant (k_r), and the non-radiative recombination rate constant (k_{nr}). To evaluate hole extraction, we performed steady-state and time-resolved photoluminescence measurements. Details on sample preparation, measurements, and data analysis are provided in Section 1.7 of the ESI† and annotated in Table S1 (ESI†). As shown in Fig. S11 (ESI†), the drastic quenching of static photoluminescence can be clearly observed for the samples with organic semiconductors. Upon excitation with a 670 nm pulsed laser, $FAPbI_3$ films modified with triphenylmethane triisocyanate deposited on glass exhibited a photoluminescence decay with an amplitude-averaged lifetime (τ) of 6.3 μs (Fig. S12A and Table S1, ESI†); the reciprocal of τ corresponds to the sum of the radiative and non-radiative rate constants ($k_r + k_{nr}$). When the surface of the $FAPbI_3$ film was coated with organic semiconductors, τ significantly decreased. Specifically, the τ

values for $FAPbI_3$ films coated with **spiro-OMeTAD**, **PTAA**, **p-TPA3Me-E**, **p-TPA3Me-E-TPAOOD-E**, and **p-TPAOOD-E** were 28 ns, 67 ns, 24 ns, 23 ns, and 22 ns, respectively (Fig. S12B–F and Table S1, ESI†). As shown in Fig. 2D, k_{he} exhibited a correlation with ΔG that can be described by Marcus electron transfer theory; the higher the HOMO energy level of the organic semiconductor, the greater the k_{he}. For these five organic semiconductors, the hole extraction yield (ϕ_{he}) was nearly 100% (Table S1, ESI†). To investigate the spatially resolved excited state characteristics of perovskite thin films coated with polystyrene or organic semiconductors, we utilized laser confocal fluorescence microscopy to image the photoluminescence lifetimes (Fig. S13, ESI†). Upon replacing polystyrene with organic semiconductors, the average photoluminescence lifetimes of the perovskite films decreased significantly, with the magnitude of the reduction following the order: **p-TPAOOD-E** > **p-TPA3Me-E-TPAOOD-E** > **p-TPA3Me-E** > **spiro-OMeTAD** > **PTAA**.

2.3 Hole density-dependent conductivity and mobility

For n–i–p type PSCs, the conductivity (σ) of the HTL significantly impacts the internal resistance of the device, and then affects fill factor and efficiency. σ is governed by both p and hole mobility (μ_p). We initially measured the σ of pristine organic semiconductor films using interdigital gold electrodes, obtaining the following values: **p-TPAOOD-E** (0.002 μS cm^{-1}) < **PTAA** (0.008 μS cm^{-1}) < **p-TPA3Me-E** (0.05 μS cm^{-1}) < **spiro-OMeTAD** (0.12 μS cm^{-1}) < **p-TPA3Me-E-TPAOOD-E** (0.24 μS cm^{-1}). Despite the slightly higher σ of **p-TPA3Me-E-TPAOOD-E**, it was still insufficient for producing high-efficiency devices when used directly as the HTL. To enhance σ, we blended these organic semiconductors with the organic salt 4-(*tert*-butyl)pyridinium 1,1,2,2,3,3-hexafluoropropane-1,3-disulfonimide (TBPH-HFSI),[55] aiming to increase the equilibrium constant of the air oxidation doping reaction by coupling anion exchange with redox reactions. As shown in Fig. 3A, σ exhibited a power-law increase with rising TBPH-HFSI weight percentages (wt%). At 15 wt% TBPH-HFSI, the σ values of the organic semiconductor composite films were: **PTAA** (13.5 μS cm^{-1}) < **p-TPAOOD-E** (25.2 μS cm^{-1}) < **p-TPA3Me-E** (34.0 μS cm^{-1}) < **spiro-OMeTAD** (44.4 μS cm^{-1}) < **p-TPA3Me-E-TPAOOD-E** (169 μS cm^{-1}).

Experimental studies showed that the capacitance of TBPH-HFSI/organic semiconductor composite films could not be accurately measured using MIS devices. The most likely reason is the dominant contribution of the SiO_2 and polybenzocyclobutene insulating layers to the total capacitance of the MIS devices compared to the organic semiconductor composite films.[56] Subsequently, we measured the electron paramagnetic resonance (EPR) spectra of the organic semiconductor films (Fig. 3B–D and Fig. S14, ESI†). As shown in Fig. S15 (ESI†), the quadratic integral of the EPR signal linearly increased with the TBPH-HFSI wt%. By comparing the EPR quadratic integrals of films with and without TBPH-HFSI, and using the p of pristine organic semiconductor films as a reference, we estimated the p of the composite films.[6] Following the principles of chemical equilibrium, the p of the organic semiconductor composite films indeed increased linearly with the TBPH-HFSI wt%; higher HOMO energy levels resulted in greater increases in p (Fig. 3E), attributed to the larger equilibrium constants of the fluorinated alkyl sulfonyl imide salt-assisted doping reactions.

With the measured σ and p, μ_p can be calculated using the equation $\sigma = \mu_p q p$, where q is the elementary charge. As shown in Fig. 3F, μ_p increased gradually with rising p. It is well known that carriers in organic semiconductors exhibit strong localization characteristics, with the density of states typically following Gaussian or exponential distributions, and transport occurring *via* thermally activated hopping.[57] As illustrated in Fig. 3G, at low densities, holes are trapped in deep traps, resulting in higher activation energy for hopping and lower μ_p; at high densities, as depicted in Fig. 3H, deep traps are

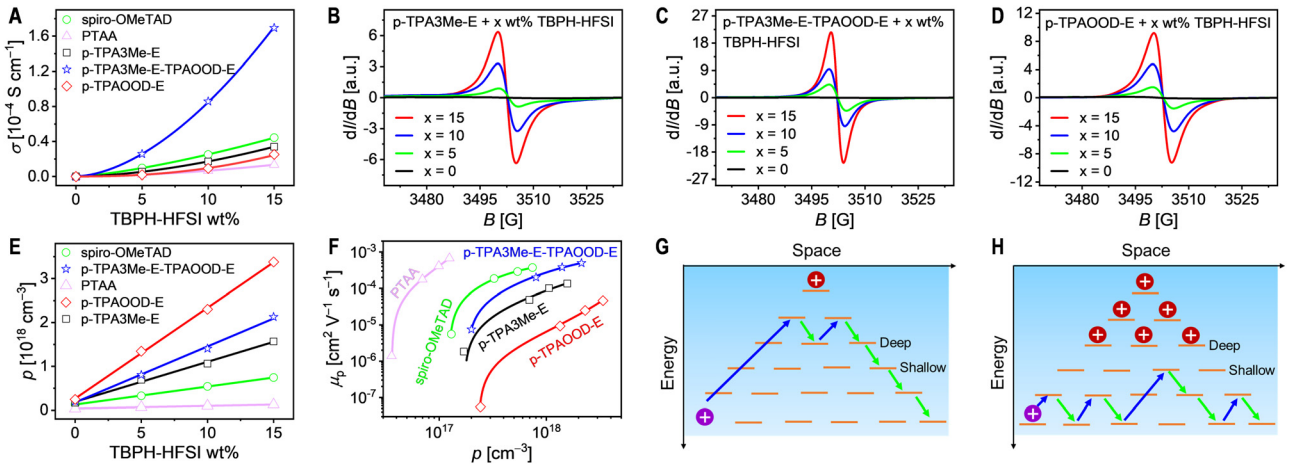

Fig. 3 (A) Electrical conductivity (σ) as a function of TBPH-HFSI weight percentages (x wt%), with solid lines indicating power-law fits. (B)–(D) Electron paramagnetic resonance spectra of triphenylamine–ethylenedioxythiophene-based polymeric semiconductor films containing varying TBPH-HFSI wt%. The first derivative of absorption intensity (dI/dB) is plotted against the magnetic field strength (B). (E) Hole density (p) as a function of TBPH-HFSI wt%, with solid lines representing linear fits. (F) Logarithmic plots of hole mobility (μ_p) *versus* p, with solid lines serving as guides to the eye. (G) and (H) Schematic illustrations of hole transport in p-type organic semiconductors *via* thermal activation hopping, where red spheres represent holes trapped in deep traps and purple spheres depict holes transported *via* multiple trapping (blue) and de-trapping (green) processes.

partially filled with holes, while the remaining holes are captured by shallow traps, leading to lower activation energy for hopping and higher μ_p.[58] Among the three triphenylamine–ethylenedioxythiophene alternating copolymers, μ_p at the same p follows the order: **p-TPAOOD-E** < **p-TPA3Me-E** < **p-TPA3Me-E-TPAOOD-E**. The low μ_p of **p-TPAOOD-E** is due to the large steric hindrance of the 2-octyldodecyloxy groups on the non-main chain phenyl rings, hindering strong π–π interactions between the conjugated backbones. In contrast, despite its lower molecular weight, **p-TPA3Me-E** exhibits higher μ_p, attributed to more favorable interchain hole transport. The μ_p of **p-TPA3Me-E-TPAOOD-E** surpasses that of **p-TPA3Me-E**, potentially due to higher molecular weight facilitating better intrachain hole transport or interchain connectivity. It is hypothesized that for **p-TPA3Me-E-TPAOOD-E**, despite half of the non-main chain phenyl rings being substituted with bulky 2-octyldodecyloxy groups, strong π–π interactions may occur between TPA3Me-EDOT segments, leading to local crossing of polymer chains.[59] Such crossing could form a network structure, providing efficient pathways for interchain charge transport. This suggests that alternating substituents can be an effective strategy to enhance the mobility of polymeric semiconductors.

Weak interactions play a critical role in the self-assembly of organic semiconductor materials, resulting in complex morphologies and structures that are difficult to characterize at atomic resolution. A variety of solid-state nuclear magnetic resonance techniques can provide valuable insights into local structures and site-specific dynamics, offering complementary information that can be correlated with data from other methods, such as X-ray scattering, vibrational and optical spectroscopies, and computational modeling. This integrative approach can provide a more comprehensive understanding of organic semiconductor structures. Although our preliminary solid-state nuclear magnetic resonance studies of the polymeric semiconductors did not yield definitive conclusions, future research could leverage advanced nuclear magnetic resonance techniques alongside complementary experimental and computational methods to establish robust structure–property relationships in these complex materials.[60]

2.4 HTL-dependent photovoltaic characteristics

We fabricated PSCs utilizing organic semiconductors blended with the doping promoter TBPH-HFSI at an 85/15 weight ratio as the HTLs, with the cell architecture depicted in Fig. S1 (ESI†). Detailed procedures for cell fabrication and testing are provided in Section 1.10 of the ESI.† The *J*–*V* curves of the cells were measured under simulated AM1.5G solar irradiation at 100 mW cm^{-2}. The statistical distribution of photovoltaic parameters (short-circuit current density, J_{SC}; open-circuit voltage, V_{OC}; fill factor, FF; power conversion efficiency, PCE) for eight cells is illustrated in Fig. S16 (ESI†). The reverse scan curves of representative cells are shown in Fig. 4A, with the corresponding photovoltaic parameters listed in Table 1. The **spiro-OMeTAD**-based cell achieved a PCE of 24.1%, attributed to its J_{SC} of 26.09 mA cm^{-2}, V_{OC} of 1.185 V, and FF of 78.0%. In contrast, the **PTAA**-based cell exhibited the lowest J_{SC} (25.54 mA cm^{-2}), V_{OC} (1.145 V), and FF (70.1%), resulting in a PCE of 20.5%. The **p-TPA3Me-E** and **p-TPAOOD-E** cells displayed very similar V_{OC}, J_{SC}, and FF, resulting in comparable PCEs of 23.2% and 23.3%, respectively. The **p-TPA3Me-E-TPAOOD-E** cell demonstrated a J_{SC} of 26.10 mA cm^{-2}, comparable to that of the **spiro-OMeTAD** cell, with the same V_{OC} of 1.185 V and the highest FF of 82.0%, achieving a PCE of 25.4%. We also measured the forward scan *J*–*V* curves and calculated the hysteresis factors. For the **p-TPA3Me-E-TPAOOD-E** cell, the hysteresis factor was 0.8% (Fig. S17, ESI†). Upon switching the bias voltage from open-circuit to maximum power point voltage, the current quickly reached a steady state, with a steady-state PCE output of 25.3% (Fig. 4B), consistent with the *J*–*V* test results. We also tested **p-TPA3Me-E-TPAOOD-E** samples with significantly low and high molecular weights, but the cell efficiency was lower, mainly attributed to lower conductivity and poorer hole transport layer morphology, respectively.

As shown in Fig. 3F, when the air doping promoter TBPH-HFSI is at 15 wt%, the μ_p of the organic semiconductor composite films follows the order: **PTAA** > **p-TPA3Me-E-TPAOOD-E** > **spiro-OMeTAD** > **p-TPA3Me-E** > **p-TPAOOD-E**. However, there is no clear correlation between μ_p and J_{SC}, suggesting that, under short-circuit conditions, the hole diffusion lengths exceed the geometric thicknesses of these hole transport layers. The **PTAA**-based cell exhibits the lowest V_{OC}, indicating the fastest interface charge recombination between the perovskite layer and the hole transport layer. Even in short-circuit conditions, rapid charge recombination can reduce the electron diffusion length in the perovskite film, resulting in a slightly lower electron collection efficiency, and consequently, a marginal reduction in J_{SC}. For cells utilizing **spiro-OMeTAD**, **p-TPA3Me-E**, **p-TPA3Me-E-TPAOOD-E**, and **p-TPAOOD-E**, the V_{OC} values are all ≥ 1.165 V, indicating slower charge recombination at the perovskite/hole transport layer interface. This allows the electron diffusion lengths in the perovskite film to exceed the geometric thickness, leading to similar J_{SC} values across these devices.

Subsequently, we measured the external quantum efficiencies (EQE) of the cells under different monochromatic light irradiations (Fig. 4C). By combining the EQE spectrum with the standard AM1.5G solar spectrum (ASTM G173-03), the short-circuit current density (J_{SC}^{EQE}) under AM1.5G conditions was predicted. The results showed that the **spiro-OMeTAD**, **p-TPA3Me-E**, **p-TPA3Me-E-TPAOOD-E**, and **p-TPAOOD-E** cells exhibited very similar EQE spectra, with nearly identical J_{SC}^{EQE} values of 25.77 mA cm^{-2}, 25.74 mA cm^{-2}, 25.78 mA cm^{-2}, and 25.76 mA cm^{-2}, respectively. In contrast, the **PTAA** cell showed a decrease in EQE in the 500–790 nm wavelength range, resulting in a J_{SC}^{EQE} of 25.23 mA cm^{-2}. This phenomenon could be related to faster recombination between electrons in the perovskite film and holes in the hole transport layer.

Next, we evaluated the electroluminescence external quantum efficiencies (EQE_{EL}) of the cells. At an injected current density of 26 mA cm^{-2}, the EQE_{EL} values for the five types of cells were as follows: **spiro-OMeTAD** (6.9%) = **p-TPA3Me-E-TPAOOD-E** (6.9%) > **p-TPA3Me-E** (4.8%) > **p-TPAOOD-E** (4.6%) > **PTAA** (2.9%) (Fig. 4D). The non-radiative V_{OC} loss (ΔV_{OC}^{nr}) was calculated using the equation $\Delta V_{OC}^{nr} = -\frac{k_B T}{q}\ln(EQE_{EL})$, where k_B is the

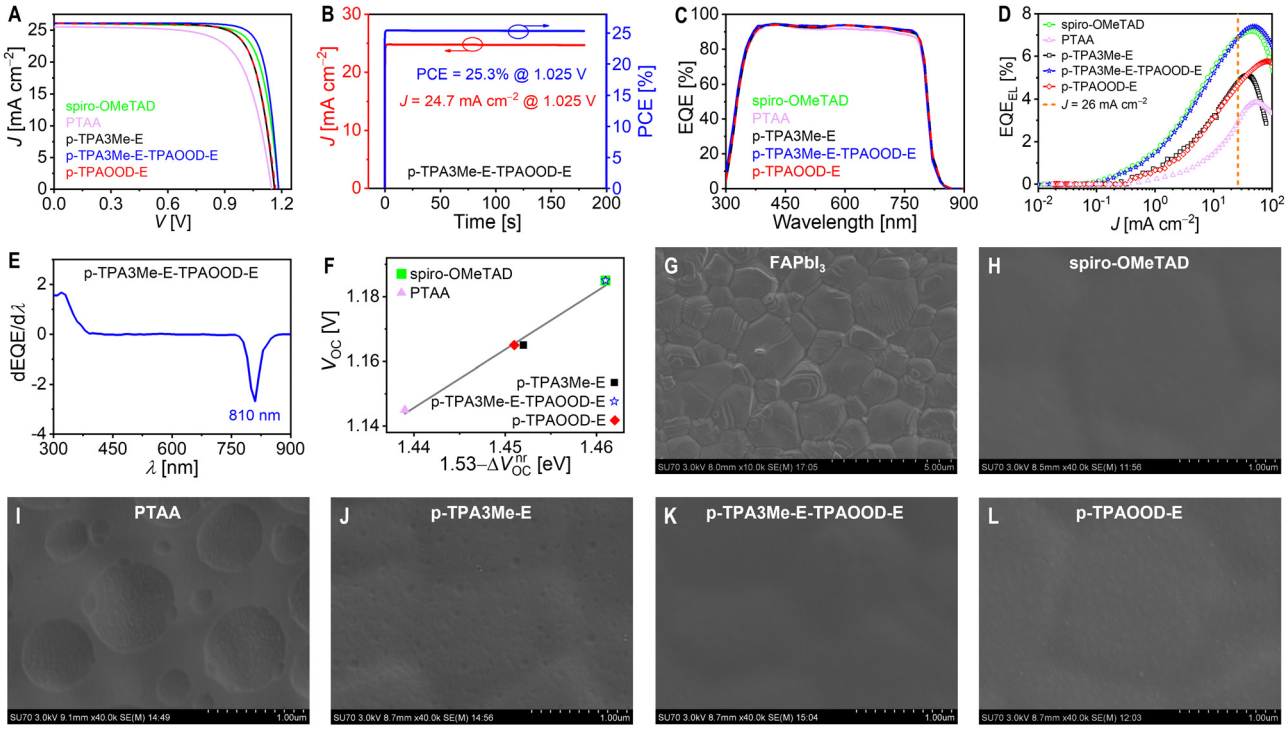

Fig. 4 (A) Reverse photocurrent density–voltage (J–V) curves of representative cells employing different hole transport layers under simulated AM1.5G irradiation at 100 mW cm^{-2}. (B) Steady-state photocurrent density (J) and power conversion efficiency (PCE) outputs of the representative **p-TPA3Me-E-TPAOOD-E** cell under AM1.5G illumination at 100 mW cm^{-2}. (C) External quantum efficiency (EQE) spectra. (D) Plots of electroluminescence external quantum efficiency (EQE$_{EL}$) as a function of injected current density (J). (E) First derivative spectrum of EQE *versus* wavelength (λ) of the **p-TPA3Me-E-TPAOOD-E** cell. The sharp peak at 810 nm can be used to calculate the optical bandgap of the $FAPbI_3$ layer (1.53 eV). (F) Relationship between open-circuit voltage (V_{OC}) and non-radiative recombination V_{OC} loss (ΔV_{OC}^{nr}). The grey solid line indicates a linear fit. (G) Scanning electron microscopy image of the $FAPbI_3$ layer in perovskite solar cells. Scale bar: 5 μm. Image was taken after removal of encapsulation materials, the gold electrode, and the hole transport layer. (H)–(L) Scanning electron microscopy images of hole transport layers in perovskite solar cells. Scale bar: 1 μm. Images were taken after removal of encapsulation materials and the gold electrode.

Boltzmann constant, T is the temperature in Kelvin, and q is the elementary charge.[61] The ΔV_{OC}^{nr} values for the five cells were **spiro-OMeTAD** (69 mV) = **p-TPA3Me-E-TPAOOD-E** (69 mV) < **p-TPA3Me-E** (78 mV) ≈ **p-TPAOOD-E** (79 mV) < **PTAA** (91 mV). By differentiating the EQE spectrum of the **p-TPA3Me-E-TPAOOD-E** cell (Fig. 4E), we estimated the optical bandgap of the perovskite absorption layer to be 1.53 eV. Furthermore, V_{OC} and $1.53 - \Delta V_{OC}^{nr}$ showed a good linear correlation (Fig. 4F); the smaller the ΔV_{OC}^{nr}, the higher the V_{OC}. The smaller non-radiative recombination losses of **spiro-OMeTAD** and **p-TPA3Me-E-TPAOOD-E** cells may be related to the integrity of HTL morphology (as discussed later). The complete morphology not only avoids direct contact between the metal electrode and perovskite, but also balances the local injection of electrons and holes, avoiding exciton quenching. Moreover, electrical impedance spectroscopy analysis (Fig. S18, ESI†) showed that the cell with **p-TPA3Me-E-TPAOOD-E** exhibited a significantly higher recombination resistance compared to **PTAA**, offering insight into the improved V_{OC}.

We then fitted the reverse scan J–V curves using the Shockley diode equation,[62] obtaining key physical parameters (Table 1): shunt resistance (R_{sh}), series resistance (R_s), and reverse saturation current (I_s). The results indicated that higher R_{sh} and lower I_s correlated with higher V_{OC}; lower R_s, higher R_{sh}, and lower I_s correlated with higher FF. R_s is apparently related to the

Table 1 Photovoltaic parameters and diode parameters of representative cells under the simulated AM1.5G irradiation[a]

Cell	J_{SC} [mA cm^{-2}]	V_{OC} [V]	FF [%]	PCE [%]	J_{SC}^{EQE} [mA cm^{-2}]	n	R_s [Ω]	R_{sh} [kΩ]	I_s [10^{-18} A]
spiro-OMeTAD	26.09	1.185	78.0	24.1	25.77	1.35	34.6	19.7	3.0
PTAA	25.54	1.145	70.1	20.5	25.23	1.49	59.8	10.2	180
p-TPA3Me-E	26.05	1.165	76.6	23.2	25.74	1.43	37.5	32.6	36
p-TPA3Me-E-TPAOOD-E	26.10	1.185	82.0	25.4	25.78	1.35	18.7	51.3	2.8
p-TPAOOD-E	26.06	1.165	76.9	23.3	25.76	1.38	42.4	31.8	11

[a] J_{SC}: short-circuit photocurrent density; V_{OC}: open-circuit voltage; FF: fill factor; PCE: power conversion efficiency; J_{SC}^{EQE}: the integral of the product of the EQE and the photo flux of the AM 1.5G emission (ASTM G173-03) over the wavelength; n: ideality factor; I_s: reverse saturation current; R_s: series resistance; R_{sh}: shunt resistance. The aperture area of metal mask: 0.07 cm^2.

conductivity of the HTL discussed in Section 2.3. High R_{sh} and low I_s may be associated with the integrity of the HTL morphology. To understand the differences in R_{sh} and I_s, we removed the encapsulation materials and gold electrode from the PSCs and imaged the HTLs. Atomic force microscopy images (Fig. S19, ESI†) revealed that the polycrystalline perovskite thin film exhibited a relatively high root-mean-square roughness of 36.8 nm. After the deposition of an HTL, the root-mean-square roughness significantly decreased in the following order: **PTAA** (25.5 nm) > **p-TPA3Me-E** (17.1 nm) > **p-TPAOOD-E** (16.4 nm) > **p-TPA3Me-E-TPAOOD-E** (14.4 nm) > **spiro-OMeTAD** (10.4 nm). Overall, atomic force microscopy imaging does not provide very valuable information to understand photovoltaic parameters. The scanning electron microscopy images showed that the HTLs based on **spiro-OMeTAD** and **p-TPA3Me-E-TPAOOD-E** were very complete and smooth (Fig. 4H and K) on the surface of the perovskite microcrystalline film (Fig. 4G). The **PTAA**-based HTL showed many pits of varying sizes, some reaching the micron scale, with a small amount of salt segregation (Fig. 4I). The **p-TPA3Me-E**-based HTL exhibited some submicron pits with a small amount of salt segregation (Fig. 4J). The **p-TPAOOD-E**-based HTL surface was rougher, with more pronounced salt segregation (Fig. 4L). The incomplete morphology of the composite HTL might facilitate micro/nano-scale contact between the gold electrode and the perovskite, introducing new charge recombination pathways, resulting in low R_{sh} and high I_s. We hypothesize that the undesirable morphology of some composite films may be due to poor miscibility between the host material and the doping promoter TBPH-HFSI. Therefore, we recorded the morphology of pure organic films used as HTLs, as shown in Fig. S20 (ESI†). It can be seen that without TBPH-HFSI, **spiro-OMeTAD** and **p-TPA3Me-E-TPAOOD-E** films remained smooth and flat; the **PTAA** film surface still exhibited pits; the **p-TPA3Me-E** film showed no pits but was not completely flat; the **p-TPAOOD-E** film surface was relatively flat. This comparison indicates that the morphology of composite films is likely controlled by the miscibility of the organic salt (doping promoter) and the organic semiconductor, a matter requiring further investigation in future research.

2.5 85 °C thermal storage stability

To assess the thermal storage stability of high-efficiency PSCs employing **spiro-OMeTAD** and **p-TPA3Me-E-TPAOOD-E**, we subjected the cells to dry air at 85 °C, periodically retrieving them for *J–V* curve measurements under AM1.5G solar illumination (100 mW cm^{-2}) at room temperature. As illustrated in Fig. 5A, after 1000 hours, the PCE retention of the **p-TPA3Me-E-TPAOOD-E** cell reached 91%, significantly surpassing the **spiro-OMeTAD** cell's retention of 68%. Fig. 5B compares the reverse scan *J–V* curves before and after 1000 hours of aging, with detailed photovoltaic parameters provided in Table S2 (ESI†). A comparative analysis of the photovoltaic parameters in Table S2 (ESI†) reveals that thermal aging resulted in a 12% decrease in J_{SC}, an 8% decrease in V_{OC}, and a 16% decrease in FF for the **spiro-OMeTAD** cell. In contrast, the **p-TPA3Me-E-TPAOOD-E** cell exhibited minimal decreases of 2.2%, 2.1%, and 5.4% in J_{SC}, V_{OC}, and FF, respectively. As depicted in Fig. 5C, the EQE maximum of the **spiro-OMeTAD** cell decreased by 9.8% after 1000 hours of thermal aging, while the **p-TPA3Me-E-TPAOOD-E** cell demonstrated a negligible decline of 1.1%.

Subsequently, we removed the encapsulation and gold electrodes from the PSCs to analyze their electronic absorption spectra (Fig. 5D). The results indicated a pronounced reduction in optical absorption for the **spiro-OMeTAD** cell, which may be associated with the decomposition of the perovskite. In

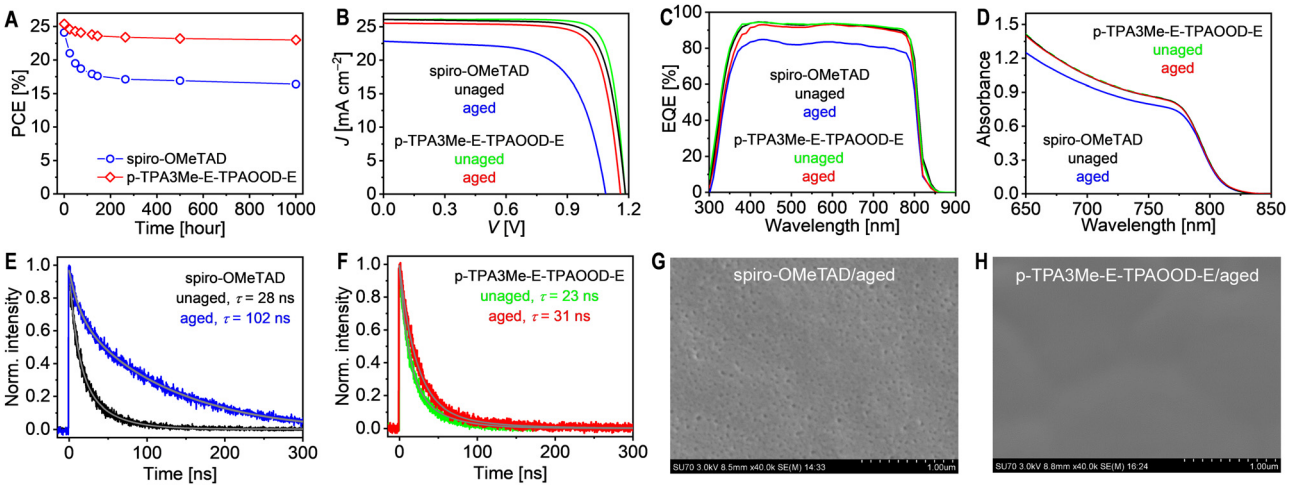

Fig. 5 (A) Evolution of power conversion efficiency (PCE) of solar cells with different hole transport layers with the time of 85 °C aging (ISOS-D-2). (B) Reverse scan photocurrent density–voltage (*J–V*) curves for cells before and after aging at 85 °C for 1000 hours, measured under 100 mW cm^{-2} simulated AM1.5G irradiation. (C) External quantum efficiency (EQE) spectra of the unaged and aged cells. (D) Electronic absorption spectra of the unaged and aged cells, with encapsulation materials and gold electrodes removed prior to measurement. (E) and (F) Time-resolved photoluminescence traces at 810 nm for the unaged and aged cells, using an excitation wavelength of 670 nm. (G) and (H) Top-view scanning electron microscopy images of the hole transport layers in the aged cells. Scale bar: 1 μm. Encapsulation materials and gold electrodes were removed before imaging.

contrast, the optical absorption of the **p-TPA3Me-E-TPAOOD-E** cell remained largely unchanged. X-ray diffraction analyses (Fig. S21, ESI†) illustrated an increase in the height of the PbI_2(001) diffraction peak after aging at 85 °C. The area of this diffraction peak in the **spiro-OMeTAD**-based cell expanded to 11.6 times its initial value, much greater than observed in the **p-TPA3Me-E-TPAOOD-E**-based cell (2.7 times). Time-resolved photoluminescence measurements revealed an increase in the lifetime (τ) of the **spiro-OMeTAD** cell from 28 ns to 102 ns (Fig. 5E), whereas the τ of the **p-TPA3Me-E-TPAOOD-E** cell increased only from 23 ns to 31 ns (Fig. 5F). This increase in τ may be linked to the formation of wide-bandgap species at the perovskite/HTL interface. Scanning electron microscopy images showed the presence of dense nanopores in the **spiro-OMeTAD**-based HTL after aging (Fig. 5G). This significant degradation of the HTL morphology may impede hole extraction and transport, potentially leading to the formation of micro- and nanoscale contacts between the perovskite and gold electrode, thereby compromising device performance. Conversely, the morphology of the **p-TPA3Me-E-TPAOOD-E**-based HTL remained intact (Fig. 5H), which may contribute to mitigating perovskite degradation under thermal stress. Further, we washed the HTL with chlorobenzene and conducted fluorescence optical microscopy imaging on the perovskite layer. For the unaged cells, no discernible patterns were observed in the perovskite layers (Fig. S22A and B, ESI†). After aging, the **spiro-OMeTAD** cell exhibited dense green luminescent spots in the perovskite layer (Fig. S22C, ESI†), likely attributed to PbI_2 luminescence. In contrast, the **p-TPA3Me-E-TPAOOD-E** cell displayed only a few small green luminescent spots (Fig. S22D, ESI†). The degradation of the perovskite may adversely affect light-harvesting efficiency and promote the formation of structural defects, leading to increased deep trap states that reduce charge separation and collection efficiencies, ultimately resulting in a deterioration of the device's photovoltaic performance. The degradation analysis highlights the crucial role of the high-T_g hole transport material in maintaining the thermal stability of n–i–p perovskite solar cells, ensuring HTL morphology stability at 85 °C and effectively mitigating the degradation of organic–inorganic hybrid lead halide perovskite films.

2.6 Humidity stability

We evaluated the humidity stability at ambient temperature of encapsulated PSCs. After 100 hours of exposure to an environment with nearly 100% humidity, the **p-TPA3Me-E-TPAOOD-E** cells retained an average of 80% of their initial PCE, significantly higher than the 50% retention observed for **spiro-OMeTAD** cells (Fig. S23, ESI†). We remark that it is necessary to identify improved encapsulation strategies to mitigate such degradation.

2.7 Operational stability

Finally, we performed maximum power point tracking (MPPT) on **spiro-OMeTAD** and **p-TPA3Me-E-TPAOOD-E** solar cells using the standard perturbation observation method. The cells, maintained in a nitrogen atmosphere, were illuminated with simulated AM1.5G solar light, while their surface temperature was controlled at 45 °C through resistive heating and semiconductor cooling. Fig. 6A–C illustrate the temporal evolution of efficiency (η_{MPP}), photocurrent density (J_{MPP}), and photovoltage

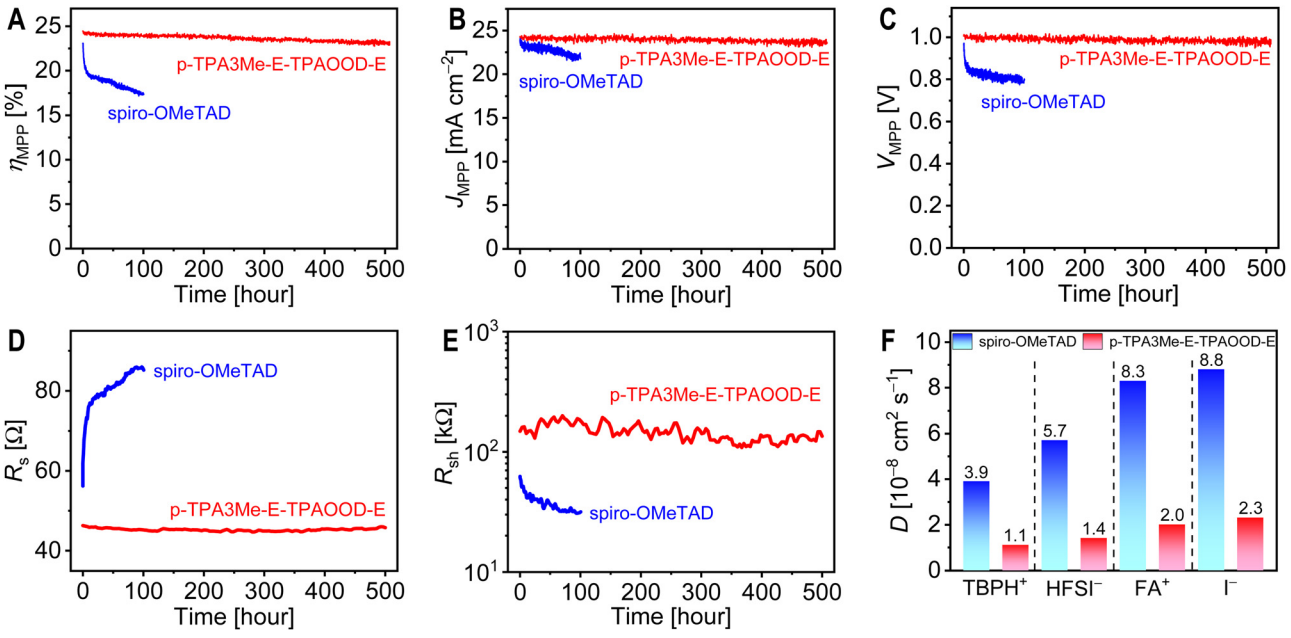

Fig. 6 (A–C) Photovoltaic parameters tracked at the maximum power point (MPP) under simulated AM1.5G irradiation at 100 mW cm^{-2}: (A) efficiency at MPP (η_{MPP}); (B) photocurrent density at MPP (J_{MPP}); (C) photovoltage at MPP (V_{MPP}). (D) and (E) Series resistance (R_s) and shunt resistance (R_{sh}) obtained from fitting the J–V curves measured intermittently during MPP tracking. (F) Ion diffusion coefficients (D) in the hole transport layer at 45 °C obtained from molecular dynamics simulations.

(V_{MPP}) at the maximum power point. Notably, after only 100 hours, the η_{MPP} of the **spiro-OMeTAD** cell decreased by 25%, corresponding to a 9.0% reduction in J_{MPP} and a 17% reduction in V_{MPP}. In stark contrast, after 500 hours, the η_{MPP} of the **p-TPA3Me-E-TPAOOD-E** cell declined modestly from 24.5% to 23.1%, resulting in an η_{MPP} retention of 94%, with J_{MPP} and V_{MPP} decreasing by 3.1% and 2.5%, respectively.

During the MPPT process, we also intermittently measured the *J–V* characteristics of the cells and fitted the data using the Shockley diode equation to obtain R_s and R_{sh}. The temporal changes in R_s and R_{sh} are depicted in Fig. 6D and E. For the **spiro-OMeTAD** cell, R_s exhibited a gradual increase over time, while R_{sh} showed a concomitant decrease. In contrast, the **p-TPA3Me-E-TPAOOD-E** cell demonstrated negligible changes in both R_s and R_{sh}. The reduction in R_{sh} suggests an accelerated charge recombination rate, likely associated with an increase in defects within the perovskite. The increase in R_s may be attributed to the accumulation of internal defects and scattering centers in the perovskite, as well as the migration of iodide ions from the perovskite to the HTL under an electric field, leading to dedoping.[63] To further investigate this phenomenon, we conducted molecular dynamics simulations to assess the diffusion behavior of relevant ions (4-(*tert*-butyl)pyridinium, $TBPH^+$; 1,1,2,2,3,3-hexafluoropropane-1,3-disulfonimide, $HFSI^-$; formamidinium, FA^+; iodide, I^-) within the two HTLs (Fig. 6F). The results indicate that these ions exhibit significantly lower diffusion coefficients in the **p-TPA3Me-E-TPAOOD-E**-based HTL with high cohesive energy density. This suppression of species diffusion within the PSC may effectively control defect formation in the perovskite layer and mitigate dedoping in the HTL.

3 Conclusions

Utilizing a direct arylation polycondensation reaction, we synthesized three triphenylamine–ethylenedioxythiophene copolymers with distinct substituents. The variation in substituents led to differences in the HOMO energy levels of the polymeric semiconductors, which subsequently influenced the extent of air oxidation doping and the rate of hole extraction from the excitonic states of the perovskite. These copolymers exhibited hole density-dependent mobility and conductivity. The synergistic combination of different substituents resulted in a more uniform morphology and enhanced hole mobility of the polymeric semiconductor composite films. These advantageous properties led to notable improvements in both the efficiency and stability of perovskite solar cells. This study offers new insights into the design strategies for high-performance polymeric semiconductors. Future research should focus on exploring alternative p-type dopants[64] for these organic semiconductors to further improve the performance of PSCs.

Data availability

The data supporting this article have been included as part of the ESI.†

Conflicts of interest

There are no conflicts to declare.

Acknowledgements

The authors thank the National Key Research and Development Program of China (No. 2022YFA1204800) and the National Natural Science Foundation of China (No. 22275160 and No. 52073250) for the financial support. The authors thank Qiaohong He, Xinyu Wang, and Linshen Chen from the Chemistry Instrumentation Center Zhejiang University for the technical support.

References

1 H.-S. Kim, C.-R. Lee, J.-H. Im, K.-B. Lee, T. Moehl, A. Marchioro, S.-J. Moon, R. Humphry-Baker, J.-H. Yum, J. E. Moser, M. Grätzel and N.-G. Park, *Sci. Rep.*, 2012, **2**, 591.
2 S. D. Stranks, G. E. Eperon, G. Grancini, C. Menelaou, M. J. P. Alcocer, T. Leijtens, L. M. Herz, A. Petrozza and H. J. Snaith, *Science*, 2013, **342**, 341.
3 M. Kim, J. Jeong, H. Lu, T. K. Lee, F. T. Eickemeyer, Y. Liu, I. W. Choi, S. J. Choi, Y. Jo, H.-B. Kim, S.-I. Mo, Y.-K. Kim, H. Lee, N. G. An, S. Cho, W. R. Tress, S. M. Zakeeruddin, A. Hagfeldt, J. Y. Kim, M. Grätzel and D. S. Kim, *Science*, 2022, **375**, 302.
4 Y. Zhao, F. Ma, Z. Qu, S. Yu, T. Shen, H.-X. Deng, X. Chu, X. Peng, Y. Yuan, X. Zhang and J. You, *Science*, 2022, **377**, 531.
5 J. Park, J. Kim, H.-S. Yun, M. J. Paik, E. Noh, H. J. Mun, M. G. Kim, T. J. Shin and S. I. Seok, *Nature*, 2023, **616**, 724.
6 Y. Ren, Y. Wei, T. Li, Y. Mu, M. Zhang, Y. Yuan, J. Zhang and P. Wang, *Energy Environ. Sci.*, 2023, **16**, 3534.
7 X. Zhao, H.-S. Kim, J.-Y. Seo and N.-G. Park, *ACS Appl. Mater. Interfaces*, 2017, **9**, 7148.
8 A. K. Jena, M. Ikegami and T. Miyasaka, *ACS Energy Lett.*, 2017, **2**, 1760.
9 Y. Wei, Y. Zhang, Y. Ren, B. Zhang, Y. Yuan, J. Zhang and P. Wang, *Adv. Funct. Mater.*, 2023, **33**, 2307501.
10 H. Su, X. Lin, Y. Wang, X. Liu, Z. Qin, Q. Shi, Q. Han, Y. Zhang and L. Han, *Sci. China: Chem.*, 2022, **65**, 1321.
11 Q. Cheng, H. Chen, F. Yang, Z. Chen, W. Chen, H. Yang, Y. Shen, X.-M. Ou, Y. Wu, Y. Li and Y. Li, *Angew. Chem., Int. Ed.*, 2022, **134**, e202210613.
12 H. Yang, T. Xu, W. Chen, Y. Wu, X. Guo, Y. Shen, C. Ding, X. Chen, H. Chen, J. Ding, X. Wu, G. Zeng, Z. Zhang, Y. Li and Y. Li, *Angew. Chem., Int. Ed.*, 2024, **63**, e202316183.
13 B. C. Thompson and J. M. J. Fréchet, *Angew. Chem., Int. Ed.*, 2008, **47**, 58.
14 Z. B. Henson, K. Müllen and G. C. Bazan, *Nat. Chem.*, 2012, **4**, 699.
15 R. Noriega, J. Rivnay, K. Vandewal, F. P. V. Koch, N. Stingelin, P. Smith, M. F. Toney and A. A. Salleo, *Nat. Mater.*, 2013, **12**, 1038.
16 H. Huang, L. Yang, A. Facchetti and T. J. Marks, *Chem. Rev.*, 2017, **117**, 10291.

17 S. Fratini, M. Nikolka, A. Salleo, G. Schweicher and H. Sirringhaus, *Nat. Mater.*, 2020, **19**, 491.
18 H. Bronstein, C. B. Nielsen, B. C. Schroeder and I. McCulloch, *Nat. Rev. Chem.*, 2020, **4**, 66.
19 Y. Zheng, S. Zhang, J. B.-H. Tok and Z. Bao, *J. Am. Chem. Soc.*, 2022, **144**, 4699.
20 Z. Peng, N. Stingelin, H. Ade and J. J. Michels, *Nat. Rev. Mater.*, 2023, **8**, 439.
21 L. Ding, Z.-D. Yu, X.-Y. Wang, Z.-F. Yao, Y. Lu, C.-Y. Yang, J.-Y. Wang and J. Pei, *Chem. Rev.*, 2023, **123**, 7421.
22 Y. Cai, Y. Zhang, J. Zhang, X. Pan, M. R. Andersson and P. Wang, *Angew. Chem., Int. Ed.*, 2024, **63**, e202315814.
23 Z. Zhu, Y. Bai, H. K. H. Lee, C. Mu, T. Zhang, L. Zhang, J. Wang, H. Yan, S. K. So and S. Yang, *Adv. Funct. Mater.*, 2014, **24**, 7357.
24 S. Ryu, J. H. Noh, N. J. Jeon, Y. C. Kim, W. S. Yang, J. Seo and S. I. Seok, *Energy Environ. Sci.*, 2014, **7**, 2614.
25 J. Lee, M. M. Byranvand, G. Kang, S. Y. Son, S. Song, G.-W. Kim and T. Park, *J. Am. Chem. Soc.*, 2017, **139**, 12175.
26 L. Zhang, C. Liu, J. Zhang, X. Li, C. Cheng, Y. Tian, A. K.-Y. Jen and B. Xu, *Adv. Mater.*, 2018, **30**, 1804028.
27 Y. Kim, E. H. Jung, G. Kim, D. Kim, B. J. Kim and J. Seo, *Adv. Energy Mater.*, 2018, **8**, 1801668.
28 L. Zhang, C. Liu, X. Wang, Y. Tian, A. K. Y. Jen and B. Xu, *Adv. Funct. Mater.*, 2019, **29**, 1904856.
29 J. Lee, G.-W. Kim, M. Kim, S. A. Park and T. Park, *Adv. Energy Mater.*, 2020, **10**, 1902662.
30 G. You, Q. Zhuang, L. Wang, X. Lin, D. Zou, Z. Lin, H. Zhen, W. Zhuang and Q. Ling, *Adv. Energy Mater.*, 2020, **10**, 1903146.
31 J. Park, S. E. Yoon, J. Lee, D. R. Whang, S. Y. Lee, S. J. Shin, J. M. Han, H. Seo, H. J. Park, J. H. Kim and B.-G. Kim, *Adv. Funct. Mater.*, 2020, **30**, 2001560.
32 Q. Fu, Z. Xu, X. Tang, T. Liu, X. Dong, X. Zhang, N. Zheng, Z. Xie and Y. Liu, *ACS Energy Lett.*, 2021, **6**, 1521.
33 H. Opoku, J. H. Lee, J.-J. Lee, H. Ahn and J. W. Jo, *ACS Mater. Lett.*, 2022, **4**, 2515.
34 Y. Bai, Z. Zhou, Q. Xue, C. Liu, N. Li, H. Tang, J. Zhang, X. Xia, J. Zhang, X. Lu, C. J. Brabec and F. Huang, *Adv. Mater.*, 2022, **34**, 2110587.
35 H.-S. Lin, T. Doba, W. Sato, Y. Matsuo, R. Shang and E. Nakamura, *Angew. Chem., Int. Ed.*, 2022, **61**, e202203949.
36 Q. Fu, H. Liu, S. Li, T. Zhou, M. Chen, Y. Yang, J. Wang, R. Wang, Y. Chen and Y. Liu, *Angew. Chem., Int. Ed.*, 2022, **61**, e202210356.
37 Q. Fu, X. Tang, H. Liu, R. Wang, T. Liu, Z. Wu, H. Y. Woo, T. Zhou, X. Wan, Y. Chen and Y. Liu, *J. Am. Chem. Soc.*, 2022, **144**, 9500.
38 X. Wang, Z. He, H. Chen, L. Yao, C. Li, X. Lin, Z. Zhou, K. Li, W. Wang, W. Cai, Q. Ling and H. Zhen, *Adv. Funct. Mater.*, 2023, **33**, 2308435.
39 S.-K. Kim, J. Kim, S. Choi, T. Yong, J. Y. Park, G. Lee, S. Han, H. R. You, S. Ko, G. Park, H. Ahn, J. Yang, Y. Kim, B. J. Kim and J. Choi, *Adv. Energy Mater.*, 2023, **13**, 2301927.
40 J. H. Heo, S. H. Im, J. H. Noh, T. N. Mandal, C.-S. Lim, J. A. Chang, Y. H. Lee, H.-J. Kim, A. Sarkar, M. K. Nazeeruddin, M. Grätzel and S. I. Seok, *Nat. Photonics*, 2013, **7**, 486.
41 Q. Jiang, Y. Zhao, X. Zhang, X. Yang, Y. Chen, Z. Chu, Q. Ye, X. Li, Z. Yin and J. You, *Nat. Photonics*, 2019, **13**, 460.
42 A. K. Mohanakrishan, P. Amaladass and J. A. Clement, *Tetrahedron Lett.*, 2007, **48**, 539.
43 K. Yamazaki, J. Kuwabara and T. Kanbara, *Macromol. Rapid Commun.*, 2013, **34**, 69.
44 F. Grenier, B. R. Aïch, Y.-Y. Lai, M. Guérette, A. B. Holmes, Y. Tao, W. W. H. Wong and M. Leclerc, *Chem. Mater.*, 2015, **27**, 2137.
45 S. Narayanan, S. P. Raghunathan, S. Mathew, M. V. M. Kumar, A. Abbas, K. Sreekumar, C. S. Kartha and R. Joseph, *Eur. Polym. J.*, 2015, **64**, 157.
46 W. Li and T. Michinobu, *Polym. Chem.*, 2016, **7**, 3165.
47 Y. Kojima, S. Hayashi and T. Koizumi, *J. Polym. Sci., Part A:Polym. Chem.*, 2017, **55**, 1183.
48 Y. Zhang, Y. Ren, X. Xie, Y. Wei, L. He, L. Fang, J. Zhang, Y. Yuan and P. Wang, *Adv. Funct. Mater.*, 2022, **32**, 2108855.
49 Z.-R. Tan, Y.-Q. Xing, J.-Z. Cheng, G. Zhang, Z.-Q. Shen, Y.-J. Zhang, G. Liao, L. Chen and S.-Y. Liu, *Chem. Sci.*, 2022, **13**, 1725.
50 A. S. Dudnik, T. J. Aldrich, N. D. Eastham, R. P. H. Chang, A. Facchetti and T. J. Marks, *J. Am. Chem. Soc.*, 2016, **138**, 15699.
51 M. M. Tepliakova, A. V. Akkuratov, S. A. Tsarev and P. A. Troshin, *Tetrahedron Lett.*, 2020, **61**, 152317.
52 M. C. Hwang, H. Kang, K. Yu, H.-J. Yun, S.-K. Kwon, K. Lee and Y.-H. Kim, *Sol. Energy Mater. Sol. Cells*, 2014, **125**, 39.
53 L. He, Y. Zhang, Y. Wei, Y. Cai, J. Zhang and P. Wang, *Matter*, 2023, **6**, 4013.
54 J. Simon and P. Bassoul, *Design of Molecular Materials. Supramolecular Engineering*, Wiley, 2000.
55 T. Li, Y. Zhang, M. Ren, Y. Mu, J. Zhang, Y. Yuan, M. Zhang and P. Wang, *Angew. Chem., Int. Ed.*, 2024, **63**, e202401604.
56 B. Yurash, D. X. Cao, V. V. Brus, D. Leifert, M. Wang, A. Dixon, M. Seifrid, A. E. Mansour, D. Lungwitz, T. Liu, P. J. Santiago, K. R. Graham, N. Koch, G. C. Bazan and T.-Q. Nguyen, *Nat. Mater.*, 2019, **18**, 1327.
57 V. Coropceanu, J. Cornil, D. A. da Silva Filho, Y. Olivier, R. Silbey and J.-L. Brédas, *Chem. Rev.*, 2007, **107**, 926.
58 H. F. Haneef, A. M. Zeidell and O. D. Jurchescu, *J. Mater. Chem. C*, 2020, **8**, 759.
59 H. Makki, C. A. Burke and A. Troisi, *J. Phys. Chem. Lett.*, 2023, **14**, 8867.
60 M. Seifrid, G. N. M. Reddy, B. F. Chmelka and G. C. Bazan, *Nat. Rev. Mater.*, 2020, **5**, 910.
61 F. Li, X. Deng, F. Qi, Z. Li, D. Liu, D. Shen, M. Qin, S. Wu, F. Lin, S.-H. Jang, J. Zhang, X. Lu, D. Lei, C.-S. Lee, Z. Zhu and A. K.-Y. Jen, *J. Am. Chem. Soc.*, 2020, **142**, 20134.
62 S. Yoo, B. Domercq and B. Kippelen, *J. Appl. Phys.*, 2005, **97**, 103706.
63 Y. Yuan and J. Huang, *Acc. Chem. Res.*, 2016, **49**, 286.
64 J. Guo, Y. Liu, P.-A. Chen, X. Wang, Y. Wang, J. Guo, X. Qiu, Z. Zeng, L. Jiang, Y. Yi, S. Watanabe, L. Liao, Y. Bai, T.-Q. Nguyen and Y. Hu, *Adv. Sci.*, 2022, **9**, 2203111.

